



**HAL**  
open science

## Phonon–glass and heterogeneous electrical transport in a-site-deficient SrTiO<sub>3</sub>

Srinivasa Rao Popuri, Rodolphe Decourt, Jason Allan McNulty, Michaël Pollet, Dominic A. Fortes, Finlay D. Morrison, Mark S. Senn, Jan-Willem G. Bos

► **To cite this version:**

Srinivasa Rao Popuri, Rodolphe Decourt, Jason Allan McNulty, Michaël Pollet, Dominic A. Fortes, et al.. Phonon–glass and heterogeneous electrical transport in a-site-deficient SrTiO<sub>3</sub>. *Journal of Physical Chemistry C*, 2019, 123 (9), pp.5198-5208. 10.1021/acs.jpcc.8b10520 . hal-02066754

**HAL Id: hal-02066754**

**<https://hal.science/hal-02066754>**

Submitted on 20 Jul 2020

**HAL** is a multi-disciplinary open access archive for the deposit and dissemination of scientific research documents, whether they are published or not. The documents may come from teaching and research institutions in France or abroad, or from public or private research centers.

L'archive ouverte pluridisciplinaire **HAL**, est destinée au dépôt et à la diffusion de documents scientifiques de niveau recherche, publiés ou non, émanant des établissements d'enseignement et de recherche français ou étrangers, des laboratoires publics ou privés.

## Phonon-glass and heterogeneous electrical transport in A-site deficient SrTiO<sub>3</sub>

S. R. Popuri,<sup>1</sup> R. Decourt,<sup>2,3</sup> J.A. McNulty,<sup>4</sup> M. Pollet,<sup>2,3,§</sup> A. D. Fortes,<sup>5</sup> F.D. Morrison,<sup>4,&</sup> M.S. Senn,<sup>6,‡</sup> and J.W.G. Bos<sup>1,\*</sup>

<sup>1</sup>*Institute of Chemical Sciences and Centre for Advanced Energy Storage and Recovery, School of Engineering and Physical Sciences, Heriot-Watt University, Edinburgh, EH14 4AS, UK.*

<sup>2</sup>*CNRS, ICMCB, 87 avenue du Dr. A. Schweitzer, Pessac F-33608, France*

<sup>3</sup>*Université de Bordeaux, 87 avenue du Dr. A. Schweitzer, Pessac F-33608, France*

<sup>4</sup>*EaStCHEM School of Chemistry, University of St Andrews, St Andrews, KY16 9ST, UK*

<sup>5</sup>*ISIS Facility, Rutherford Appleton Laboratory, Harwell Campus, Didcot, OX11 0QX, UK*

<sup>6</sup>*Department of Chemistry, University of Warwick, Gibbet Hill, Coventry, CV4 7AL, UK*

Corresponding author: \*: [j.w.g.bos@hw.ac.uk](mailto:j.w.g.bos@hw.ac.uk)

§: [michael.pollet@icmcb.cnrs.fr](mailto:michael.pollet@icmcb.cnrs.fr); &: [finlay.morrison@st-andrews.ac.uk](mailto:finlay.morrison@st-andrews.ac.uk); ‡: [m.senn@warwick.ac.uk](mailto:m.senn@warwick.ac.uk);

The phonon-glass electron crystal concept is one of the key guiding principles for the development of efficient thermoelectric materials. Here, we confirm that SrTiO<sub>3</sub> with vacancies on the perovskite A-site is a phonon-glass for 27% A-site vacancies. Furthermore, we find that these samples are electrically inhomogeneous with a core-shell grain structure that limits the electron crystal properties. Thermal conductivity, heat capacity and neutron powder diffraction, complemented by representational analysis and phonon calculations, were used to investigate the thermal transport. This reveals that the heat carrying modes are dominated by Sr motions and that these become more localised upon the introduction of the A-site vacancies. Impedance spectroscopy and DC electrical measurements were used to probe the heterogeneous electrical structure of insulating and conducting samples. This reveals the coring of grains due to oxidation on cooling from sintering temperatures. The resultant insulating shell limits the thermoelectric power factor to  $S^2/\rho = 0.45$  mW m<sup>-1</sup> K<sup>-2</sup> and the figure of merit to  $ZT = 0.15$  at 900 K for Sr<sub>0.20</sub>La<sub>0.53</sub>□<sub>0.27</sub>Ti<sub>0.95</sub>Nb<sub>0.05</sub>O<sub>3-δ</sub>. The thermal properties of these materials are therefore controlled by an intrinsic feature of the microstructure (i.e. the A-site vacancies), while the electrical properties are grain boundary limited, which in principle can be controlled independently to raise  $S^2/\rho$  and  $ZT$ .

## Introduction

The design of phonon glass electron crystal (PGEC) materials has been one of the key guiding concepts of modern thermoelectrics research.<sup>1</sup> The aim is to create materials with the good electrical properties of crystalline solids but with the low thermal conductivity of a structural glass. If this can be achieved, then high thermoelectric figures of merit,  $ZT = (S^2/\rho\kappa)T$  and efficient waste heat recovery become possible.<sup>2-3</sup> Here,  $S$  is the Seebeck coefficient,  $\rho$  is the electrical resistivity and the thermal conductivity  $\kappa$  is the sum of lattice and electronic components. Classical examples of PGEC materials are host-guest materials,<sup>4-7</sup> such as clathrates and skutterudites that consist of a framework for electrical conduction and loosely bound rattling atoms that reduce the thermal conductivity. The rattler ions lead to a low-energy non-dispersive mode in the phonon bandstructure, which causes an avoided crossing and lowers the group velocity of the heat carrying acoustic modes.<sup>8-10</sup> The observation of Einstein modes in heat capacity is often a key indicator for these localised vibrations.

$\text{SrTiO}_3$  is one of the best explored oxide thermoelectric materials with peak  $ZT = 0.4$  at high temperatures.<sup>11-18</sup> It is characterised by large power factors  $S^2/\rho \leq 3 \text{ mW m}^{-1} \text{ K}^{-2}$  at  $\sim 500 \text{ K}$  in single crystals,<sup>19-20</sup> which is competitive with many of the best semiconductor thermoelectrics. The limitation is the relatively large  $\kappa_{\text{lat}} \sim 10 \text{ W m}^{-1} \text{ K}^{-1}$  near room temperature,<sup>21-22</sup> which is far larger than  $\kappa_{\text{lat}} \sim 1 \text{ W m}^{-1} \text{ K}^{-1}$  that is desirable to achieve high  $ZT$  values. For this reason, great effort has been expended to reduce  $\kappa_{\text{lat}}$  via substitutions on the Sr, Ti and sites and through oxygen deficiency.<sup>23-25</sup> This work has led to a substantial reduction to  $\kappa_{\text{lat, RT}} \sim 3-4 \text{ W m}^{-1} \text{ K}^{-1}$  but always maintained a  $T^{-z}$  temperature dependence,<sup>26</sup> typical of crystalline materials. Recently, we used Sr vacancies to manipulate the thermal transport via the perovskite A-site, while leaving the conducting Ti-O framework unaffected.<sup>22, 27</sup> This sublattice engineering resulted in controlled transition to a glass-like  $\kappa$  for 27% vacancies with a nearly temperature independent value of  $\sim 2.5 \text{ W m}^{-1} \text{ K}^{-1}$ . This value is close to the predicted minimum  $\kappa$  for  $\text{SrTiO}_3$ .<sup>22</sup> The introduction of Sr

vacancies leads to a large mass disorder parameter  $\Gamma = 0.49$  for 27% vacancies, which is far larger than attained by conventional alloying (e.g. mixing Sr and La with  $\Gamma_{\max} = 0.08$ ), suggesting that structural disorder is an important factor. However, at the same time, a large fraction of the Sr-O chemical bonds is broken, and this is expected to lead to an Einstein-like localisation of phonon modes involving Sr. Although the high-temperature data signalled a dramatic change in  $\kappa(T)$ ,<sup>22</sup> confirmed by other groups,<sup>13, 28-30</sup> low-temperature data are needed to confirm the suppression of the peak in  $\kappa(T)$ , which signals the emergence of a phonon-glass. Recently, a near identical transition to phonon-glass behaviour was observed in  $\text{Na}_{0.5}\text{La}_{0.5}\text{TiO}_3$ ,<sup>31</sup> where Sr has been replaced by an equal mixture of  $\text{Na}^+$  and  $\text{La}^{3+}$ . This leads to a similar mass disorder parameter ( $\Gamma = 0.54$ ) but phonon calculations also point towards a localisation of the lattice vibrations due to the highly divergent (weak/strong) Na-O and La-O bond strengths.

In terms of the electron crystal properties, our earlier results showed a reduction in  $S^2/\rho$  as the amount of A-site vacancies is increased.<sup>22, 27</sup> For example, samples with 7% vacancies were found to have  $S^2/\rho = 1.3 \text{ mW m}^{-1} \text{ K}^{-2}$  at 500 K, which decreased to  $\sim 0.15 \text{ mW m}^{-1} \text{ K}^{-2}$  at 800 K for 27% vacancies. The suppression of the  $\sim 500 \text{ K}$  peak is caused by the appearance of a semiconducting tail near room temperature, which is absent for small amounts of vacancies. A nearly identical optimisation of  $S^2/\rho$  and ZT near 5-10% vacancies was found by Lu et al.<sup>13</sup> The  $\text{Na}_{0.5}\text{La}_{0.5}\text{TiO}_3$  phonon-glass system without A-site vacancies has similar  $S^2/\rho$  and ZT  $\sim 0.20$ , compared to a  $\text{SrTiO}_3$  reference sample, demonstrating that it is possible to combine phonon-glass and electron crystal properties in  $\text{SrTiO}_3$  based perovskites.<sup>31</sup>

In this manuscript, we confirm the presence of a vacancy induced phonon-glass state in  $\text{SrTiO}_3$  and provide insight into its origins. Heat capacity measurements demonstrate an increase in Einstein character at low energies, signalling a flattening and localisation of phonon modes. In addition, we reveal the presence of a heterogeneous core-shell grain structure. This suppresses the electron crystal properties due to the presence of an oxidised shell, which forms on cooling from high-temperature sintering conditions and increases the electrical resistivity.

## Experimental

Polycrystalline  $\text{Sr}_{1-x}\text{La}_{0.67x}\text{Ti}_{0.33x}\text{TiO}_3$  ( $x = 0, 0.4$  and  $0.8$ ) samples were prepared on a 3-gram scale by heating cold pressed pellets containing ground mixtures of  $\text{SrCO}_3$  (Alfa Aesar, 99.99%),  $\text{La}_2\text{O}_3$  (Sigma-Aldrich 99.99%) and  $\text{TiO}_2$  (Alfa Aesar, 99.99%) at  $1200^\circ\text{C}$  for two times 12 hours, and at  $1400^\circ\text{C}$  for 4 hours in air, with intermediate regrinding between steps. 1% excess  $\text{SrCO}_3$  was used for the  $x = 0.4$  and  $x = 0.8$  samples. Oxygen deficient and Nb substituted

$\text{Sr}_{0.20}\text{La}_{0.53}\text{Ti}_{1-y}\text{Nb}_y\text{O}_{3-\delta}$  ( $0 \leq y \leq 0.15$ ;  $\text{Nb}_2\text{O}_5$  from Alfa Aesar, 99.9985%) samples were prepared in a similar manner but all heating steps were done under 5%  $\text{H}_2$  in  $\text{N}_2$  with the samples placed on graphite disks. The final heating step for these two samples was  $1450^\circ\text{C}$  for 4 hrs. The densities of the sintered pellets are 92-97% of the theoretical values (see Table S1).

Laboratory X-ray powder diffraction data were collected on a Bruker D8 Advance diffractometer with  $\text{Cu K}\alpha_1$  radiation. X-ray diffraction patterns (8 hr data collection) for all samples are shown in Fig. S1 in the Supplementary Information. The microstructure and homogeneity of a  $\text{Sr}_{0.2}\text{La}_{0.53}\text{Ti}_{0.27}\text{TiO}_3$  sample sintered in air was examined using a Quanta 650 FEG Scanning Electron Microscope. This showed the sample to be well sintered with large grains and a uniform elemental distribution (Fig. S2).

Temperature dependent neutron powder diffraction (NPD) data were collected on an 8-gram  $\text{Sr}_{0.2}\text{La}_{0.53}\text{Ti}_{0.27}\text{TiO}_3$  sample (sintered in air) using the time-of-flight High Resolution Powder Diffractometer (HRPD), equipped with a closed-cycle refrigerator (4-290 K) and furnace (300-1000 K), at the ISIS neutron and muon source, UK. Rietveld fits were performed using the GSAS/EXPGUI programmes.<sup>32</sup>

Low-temperature thermal conductivity measurements were made using the Thermal Transport Option of a Quantum Design Physical Property Measurement System (PPMS). The heat capacities of  $\text{SrTiO}_3$  and  $\text{Sr}_{0.2}\text{La}_{0.53}\text{Ti}_{0.27}\text{TiO}_3$  (both sintered in air) were measured between 2 and 300 K using the heat capacity option of the PPMS. High temperature thermal diffusivity ( $\alpha$ ) and heat

capacity ( $C_p$ ) were measured using a Netzch LFA 457 and Perkin Elmer DSC 8500. The thermal conductivity was evaluated from the heat capacity and diffusivity data using:  $\kappa = \alpha(T)C_p(T)d$ , where  $d$  is the sample density. Electrical resistivity and Seebeck measurements were made using a Linseis LSR-3 instrument under a He atmosphere. Impedance spectroscopy was carried out on ceramic pellets over the frequency range 5 Hz - 13 MHz using an HP4192A Impedance Analyser under an applied ac voltage of 100 mV. Ag paint electrodes (RS components) were applied to opposing pellet faces and cured at 120 °C for 20 minutes. Samples were mounted in a sample holder of in-house design and placed in a non-inductively wound tube furnace allowing data to be collected from ambient to 923 K. All data were subsequently corrected for sample geometry (electrode area and sample thickness); as a result, resistance ( $R$ ) values extracted by modelling on equivalent circuits consisting of RC elements (discussed below) correspond to resistivities.

Symmetry analysis of the atomic displacement at the high-symmetry points in the Brillouin zone were done using the web based program ISODISTORT using the  $Pm-3m$  perovskite, with a setting placing the A-site at the origin of the unit cell as the parent reference structure.<sup>33</sup> Phonon Eigen vector and values of high symmetry SrTiO<sub>3</sub> were calculated using CASTEP<sup>34</sup> in the density functional perturbation theory (DFPT) approximation<sup>35</sup> for 28 points in reciprocal space. For the DFT calculations we used the GGA PBEsol exchange correlation functional<sup>36</sup> with norm-conserving pseudo potentials with a plane wave basis set cut-off energy of 600 eV and an  $8 \times 8 \times 8$  k-grid with respect to the cubic cell. The relaxed cell volume after geometry optimisation was 3.880995 Å<sup>3</sup>. The change in unit cell stress was less than 0.015 GPa in the final optimisation cycle. A custom written script was used to plot the phonon dispersion curves with grey-scale weightings reflecting the magnitude of the projected atomic displacements according to the Eigen vectors as calculated by DFPT.

## Results

### Thermal properties

*Thermal conductivity:* Combined low- and high-temperature  $\kappa(T)$  data for a selection of  $\text{Sr}_{1-x}\text{La}_{0.67x}\text{Ti}_{0.33x}\text{Ti}_{1-y}\text{Nb}_y\text{O}_{3-\delta}$  samples with 0% ( $x = 0$ ), 13% ( $x = 0.4$ ) and 27% ( $x = 0.8$ ) vacancies are shown in Figure 1. The  $\kappa(T)$  measurements confirm the suppression of the 25 K peak in  $\kappa(T)$  and the emergence of phonon-glass state for the samples with 27% vacancies. Only marginal differences are evident between the 27% A-site vacancy samples sintered in air (labelled with  $\text{O}_3$ ) and under 5%  $\text{H}_2$  in  $\text{N}_2$  (labelled with  $\text{O}_{3-\delta}$ ), suggesting that any oxygen vacancies have a minimal impact on  $\kappa(T)$ , and that the A-site vacancies are the key driver for the phonon-glass state. In all cases, the electronic contribution to  $\kappa$  is negligibly small due to the relatively high  $\rho(T)$  of these samples (see below).

*Phonon Eigen Vector Analysis:* Symmetry analysis was used to obtain information on which atomic displacements contribute to the various phonon Eigen vectors at the high symmetry points in the Brillouin zone (BZ). These modes are visualised in Figure 2 and an overview of the atoms that are allowed by symmetry to enter in to the various characters of the Eigen vectors at the high-symmetry points are given in Table 1. This analysis reveals that the modes that corresponds to Eigen vectors of character  $\text{R}_4^-$ ,  $\text{M}_3^-$ ,  $\text{M}_5^-$ ,  $\text{X}_3^-$  and  $\text{X}_5^-$  points contain Sr displacements and can therefore be expected to be strongly affected by the vacancy engineering. Furthermore, as the characters of the phonon Eigen vectors are expected to vary continuously, lines of dispersion connecting these points, (e.g.  $\text{X}_5^-$  to  $\text{R}_4^-$  and  $\Gamma$  to  $\text{X}_3^-$ ) will also have Eigenvectors that are dominated by A-site displacements even though by symmetry, the character of the different atoms are now allowed to mix (see Table 2). To validate this assertion, the symmetry analysis results are compared to our atom resolved calculations of the phonon dispersion, which are shown in Figure 2. This reveals that most of the phonon density of states below  $130 \text{ cm}^{-1}$  can be attributed to a single band of low-energy modes that are essentially of Sr nature with only minor Ti and O admixture. While at the zone boundaries the group velocity of the phonon modes will clearly be zero, the fact that they have significant dispersion across the BZ, means that they are expected to have a substantial effect on the low temperature thermal transport properties of the system that we study here. Indeed, the calculated 300 K cumulative  $\kappa_{\text{lat}}$

from Ref. 37, replotted in Figure 2, alongside our atom resolved phonon dispersion curves, reveals that up to 50% of the lattice conductivity is attributable to phonon modes of energy  $<130 \text{ cm}^{-1}$ , and that this is dominated by phonons with predominantly Sr character. As noted before,<sup>37</sup> some of the optic modes have considerable dispersion and therefore contribute to the thermal transport. Many of these heat conducting modes are dominated by Ti motions, and are mainly at higher energies. Oxygen contributes to most of the modes throughout the BZ (in keeping with the symmetry analysis in Tables 1, 2). It should be noted that the imaginary frequencies at the R-point are due to an instability related to an octahedral rotation present as a structural distortion (Pm-3m to I4/mcm) below 110 K. The main result is hence a very striking low-energy mode that is dominated by Sr motions, which can be expected to be strongly affected and localised by the disruption of the Sr-O bonding network.

*Heat capacity:*  $C_p$  data (2-873 K) for  $\text{SrTiO}_3$  and  $\text{Sr}_{0.8}\text{La}_{0.53}\square_{0.27}\text{TiO}_3$  (sintered in air) are shown in Figure 3. These data were fitted using a small electronic contribution ( $\gamma T$ ) and a combination of two Debye ( $\theta_{D_i}$ ) and two Einstein ( $\theta_{E_i}$ ) modes with the total number of oscillators equal to the number of atoms per formula unit (i.e.  $\sum n_i = 5$  for  $x = 0$  and  $\sum n_i = 4.73$  for  $x = 0.8$ ):<sup>38</sup>

$$C_p = \gamma T + \sum_{i=1}^2 \left[ 9n_{D_i} R \left( \frac{T}{\theta_{D_i}} \right)^3 \int_0^{\theta_{D_i}/T} \frac{x^4 e^x}{(e^x - 1)^2} dx \right] + \sum_{i=1}^2 \left[ 3n_{E_i} R \left( \frac{\theta_{E_i}}{T} \right)^2 \frac{e^{\theta_{E_i}/T}}{(e^{\theta_{E_i}/T} - 1)^2} \right] \quad (1)$$

The energies and weighting of these modes are summarized in Table 3 and the quality of the fits is evident from the  $C_p(T)$ ,  $C_p/T^3(T)$  and  $C_p/T(T^2)$  plots in Figure 3. The lowest energy Einstein mode ( $\theta_{E2} = 17\text{-}19 \text{ K}$ ) accounts for the peak at  $\sim 4 \text{ K}$  (Figure 3c, d). This mode has a low weighting ( $n_{E2} < 0.001$ ) and won't be discussed any further. The weighting of the high-energy Debye mode ( $n_{D1} \sim 3.1$ ) does not change significantly between the two samples, while it softens from 676(3) K to 617(5) K, in agreement with the presence of vacancies and increased flexibility of the structure. For  $\text{SrTiO}_3$ :  $\theta_{D2} = 249(1) \text{ K}$  ( $n_{D2} = 1.8$ ) and  $\theta_{E1} = 166(1) \text{ K}$  with a low  $n_{E1} = 0.1$ . These values change to  $\theta_{D2} = 223(1) \text{ K}$  with a reduced  $n_{D2} = 1.1$  and  $\theta_{E1} = 175(1) \text{ K}$  with a five-fold increased  $n_{E1} = 0.5$ , signalling a transfer of spectral weight from Debye into more localised Einstein modes, for the

phonon-glass sample. The weighted average of the Debye and Einstein temperatures (using  $\theta_E/\theta_D \approx \sqrt[3]{\pi/6}$ ) decreases from 514(2) to 488(2) K, consistent with a softening of the lattice. The low-temperature  $C_p/T(T^2)$  data are shown in Figure 3e, f and evidence significant non-linearity due to the low-energy  $\theta_{E2}$  modes. The fitted values for the Sommerfeld coefficient are  $\gamma = 0.2 \text{ mJ mol}^{-1} \text{ K}^{-2}$  for  $\text{SrTiO}_3$  and  $\gamma = 0.5 \text{ mJ mol}^{-1} \text{ K}^{-2}$  for  $\text{Sr}_{0.8}\text{La}_{0.53}\square_{0.27}\text{TiO}_3$ . This suggests a non-zero density of states at the Fermi Level,  $N(E_F) \neq 0$ , despite these samples being electrically insulating when probed by DC methods. However, as discussed below, impedance measurements indicate the presence of a conducting core - insulating shell microstructure, consistent with  $\gamma \neq 0$ .

*Atomic displacement parameters:* Variable temperature NPD data (4-1000 K) were collected from a  $\text{Sr}_{0.20}\text{La}_{0.53}\square_{0.27}\text{TiO}_3$  sample sintered in air. A representative Rietveld fit to the 300 K dataset is shown in Figure 4a. The sample undergoes a structural phase transition from the simple cubic Pm-3m perovskite to a tetragonal I4/mcm superstructure between 473-573 K (Fig. S3). The I4/mcm structure is characterised by  $a^0a^0c^-$  octahedral tilting<sup>39</sup> with no evidence for the ordering of the A-site vacancies in vacancy-rich and poor layers.<sup>40-41</sup> The temperature dependence of the isotropic thermal displacement parameters ( $U_{iso}$ ) for the Sr/La, Ti and O sites is given in Figure 4b. This plot shows that all atomic sites have significant residual disorder at 4 K, indicating that the Sr vacancies affect the Ti and O sublattices. To facilitate fits to the  $U_{iso}(T)$ , a weighted average of the O  $U_{iso}$ 's on the 4c and 8d sites of the I4/mcm structure was calculated. Fits were undertaken using both the Debye and Einstein models:<sup>42-43</sup>

$$U_{iso} = \frac{3\hbar^2}{mk_B\theta_D} \left[ \frac{1}{4} + \left( \frac{T}{\theta_D} \right)^2 \int_0^{\theta_D/T} \frac{x}{e^x - 1} dx \right] + d^2 \quad (2)$$

$$U_{iso} = \frac{\hbar^2}{2mk_B\theta_E} \coth \frac{\theta_E}{2T} + d^2 \quad (3)$$

The best fit to the A-site  $U_{iso}$ 's was obtained using the Einstein model, which had a ~10% lower residual, whereas the Debye model yielded slightly better fit statistics for the Ti and O sites but with little visual difference in fit quality. The presence of a significant Einstein contribution to at least one of the  $U_{iso}$ 's is consistent with the heat capacity fits. The final fitted values are:  $\theta_E = 150(5) \text{ K}$

(Sr/La) [ $\theta_D = 260(10)$  K (Sr/La)],  $\theta_D = 488(11)$  K (Ti) and  $\theta_D = 664(11)$  K (O). The  $\theta_E = 150(5)$  K for Sr/La is in good agreement with  $\theta_{E1} = 175(1)$  K from  $C_p$  fitting, suggesting that the A-site vibrations do indeed start to become more localised. A fit to the average  $U_{iso}$  for the compound, yielded  $\theta_D = 454(9)$  K, in good agreement with the weighted average from the  $C_p(T)$  fits ( $\theta_{D, av} = 488(2)$  K). The residual disorder ( $d^2$ ) values did not vary between the Debye and Einstein fits and are  $d^2 = 0.0060(2)$  Å<sup>2</sup> (Sr/La),  $d^2 = 0.0095(2)$  Å<sup>2</sup> (Ti) and  $d^2 = 0.0124(2)$  Å<sup>2</sup> (O). As can be seen from the inset to Fig. 4c, the  $d^2$  values have a linear dependence on the distance to the A-site, confirming that the atoms nearest to the A-site vacancies (O) are affected most strongly by structural disorder.

### Electrical properties

This section is split into two parts: the first deals with impedance spectroscopy measurements on electrically insulating  $Sr_{0.2}La_{0.53} \bullet_{0.27}TiO_3$  samples sintered in air and under flowing oxygen. The second part is focussed on the electrical properties of highly conducting  $Sr_{0.20}La_{0.53} \square_{0.27}Ti_{1-y}Nb_yO_{3-\delta}$  samples sintered under 5%  $H_2$ . Both sets of results point towards an inhomogeneous core-shell microstructure.

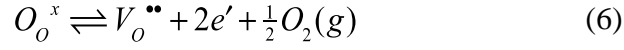
*Insulating samples:* Immittance spectroscopy (IS) data for  $Sr_{0.2}La_{0.53} \bullet_{0.27}TiO_3$  sintered in air indicated it to be highly insulating with  $\rho \gg 10^7$  Ω cm at 300 K. Despite the noise due to the high sample impedance, a single semi-circular arc was observed in the complex modulus ( $M^*$ ) plane plot, with a corresponding Debye-like peak in the imaginary modulus ( $M''$ ) spectroscopic plot, Fig 5a. Analysis using a parallel RC element shows that this response has a capacitance,  $C \sim 10$  pF and  $\rho \sim 0.21$  MΩ cm at 300 K. The magnitude of  $C$  is typical of a bulk response for a non-ferroelectric material,<sup>44</sup> *i.e.* it represents a significant volume fraction of the sample. The size of the semi-circular arc and the  $M''$  peak height remained invariant upon heating, indicating that the capacitance is relatively temperature independent. However, the  $M''$  peak was displaced to higher frequency, indicating a decrease in time constant due to a decrease in  $\rho$ , Fig 5a. As the semi-circular arc was

increasing hard to fully resolve,  $C$  and  $\rho$  were estimated from the  $M''$  peak at each temperature according to:

$$C = \frac{\epsilon_0}{2M''_{max}} \quad (4)$$

$$\rho = \frac{1}{2\pi f_{max}C} \quad (5)$$

where  $\epsilon_0$  is the vacuum permittivity,  $M''_{max}$  is the imaginary modulus peak height and  $f_{max}$  is the frequency (in Hz) at which the peak maximum occurs.<sup>45</sup> Using this methodology conductivity values for the bulk response,  $b1$  ( $\sigma_{b1} = 1/\rho_{b1}$ ) were determined at each temperature at which a peak maximum was observed. The values exhibit the expected Arrhenius behaviour with an activation energy,  $E_A \sim 0.33$  eV, see Fig 6. On further heating to above 700 K a further semi-circular arc appears in both the complex impedance ( $Z^*$ , Fig. 5c) and modulus ( $M^*$ ) plane plots with corresponding Debye-like peaks in the  $Z''$  and  $M''$  spectroscopic plots, Fig. 5b. The peaks are spectroscopically coincident, Fig 5b, and have an associated  $C \sim 3$  pF at all temperatures analysed, indicating that this is associated with a bulk-like (high volume fraction) region of the sample – assigned as  $b2$  hereafter. With increasing temperature two lower frequency responses are increasingly evident in the impedance data, Fig 5c, d; these responses have associated  $C$  of the order  $10^{-10}$  and  $10^{-8}$  F and are assigned to grain boundary and electrode responses, respectively. These responses contribute very little to the total sample resistivity,  $\rho_T$ , and to a first approximation  $\rho_T \approx \rho_{b2}$  (and hence  $\sigma_T \approx \sigma_{b2}$ ).  $\rho_{b2}$  and  $C_{b2}$  values were extracted from  $Z^*$  plane plots based on a simple parallel RC model and  $\sigma_{b2}$  plotted as function of temperature in Arrhenius format, Fig 6. The data indicate a thermally-activated conductivity with  $E_A \sim 1.40$  eV. Overall the data indicate an electrical microstructure with coexistence of two high volume fraction regions within the sample and which have significantly different conductivity. Such a microstructure, often referred to as “coring”, is well known to occur in titanate dielectrics,<sup>46</sup> whereby oxygen is lost during high temperature sintering releasing (conduction) electrons:



On cooling, and post densification, slow diffusion kinetics mean that these oxygen vacancies are not filled homogeneously and can result in either a semiconducting pellet interior with an insulating “skin”, or semiconducting grain interiors with an oxidised (insulating) grain shell.<sup>45</sup> In the case of the former, polishing can remove this layer. In our case, polishing of the sample had no effect on the IS data indicating the latter microstructure, see Fig 6 inset. Such coring effects are not detectable by conventional DC conductivity measurements but are often visually evident by a dark grey-blue colouring below a lighter yellow-beige surface; the effect can also be exacerbated by pressing defects.<sup>46</sup> By contrast IS data for  $Sr_{0.2}La_{0.53} \bullet_{0.27}TiO_3$  sintered in  $O_2$  at 1400 °C indicates an electrically homogenous microstructure with no evidence of a conductive core. The impedance and modulus data obtained above 700 K are dominated by a single response, with associated capacitance of *ca.* 8-9 pF, characteristic of a bulk response (Figure S4).<sup>44</sup> As with the air-sintered sample, grain boundary and electrode effects make a small contribution to the total sample resistance but over the temperature range studied  $\sigma_T \approx \sigma_b$ . The bulk conductivity ( $\sigma_b$ ) exhibits Arrhenius behaviour with  $E_A \sim 1.41$  eV – very similar in both magnitude and temperature dependence to the resistive (shell) response in the air-sintered sample, Fig 6.  $Sr_{0.2}La_{0.53} \bullet_{0.27}TiO_3$  and  $Sr_{0.2}La_{0.53} \bullet_{0.27}Ti_{1-y}Nb_yO_{3-\delta}$  sintered in 5%  $H_2$  in  $N_2$  were too conductive to allow deconvolution of their electrical microstructure using immittance spectroscopy.

*Conducting samples:*  $S(T)$ ,  $\rho(T)$ , the power factor  $S^2/\rho$  and ZT for several

$Sr_{0.20}La_{0.53} \square_{0.27}Ti_{1-y}Nb_yO_{3-\delta}$  samples ( $0 \leq y \leq 0.15$ ) sintered under 5%  $H_2$  are shown in Figure 7.

Small amounts of Nb substitution are known to improve  $S^2/\rho$ . The largest  $S^2/\rho = 0.55$  mW m<sup>-1</sup> K<sup>-2</sup> (from 600-1000 K) was observed for the  $y = 0.05$  sample. This is 2-3 times smaller than the best reported values for polycrystalline  $SrTiO_3$  based thermoelectrics, thus limiting ZT to  $\sim 0.15$  at 873 K, despite the reduction of  $\kappa(T)$  and emergence of a phonon-glass state by the introduction of A-site

vacancies. We note that  $S^2/\rho$  increases monotonously and does not show a peak at  $\sim 500$  K, which is caused by the semiconducting  $\rho(T)$  near room temperature.

Another important observation is the non-monotonous relation between electrical conductivity,  $\sigma = 1/\rho$ , and  $S$ . Within a single band approximation, increases in  $S$  are linked to a reduction in carrier concentration,  $n$ , thus leading to a reduction in  $\sigma = ne\mu$ , where  $e$  is the electron charge and  $\mu$  is the carrier mobility. For the current materials, there is no systematic  $S(\sigma)$  dependence and an almost random variation is observed (Table 4). This non-systematic variation, can be explained using a core-shell model, analogous to the samples sintered in air. Here, the shell occurs due to an increase in partial oxygen pressure upon cooling from sintering conditions under 5%  $H_2$  in  $N_2$ , leading to oxidation of the outer layer of the grains.<sup>47</sup> In a two-component model electrically connected in series,  $S$  and  $\rho$  are given by:<sup>48</sup>

$$S = \frac{(1-x_s)\frac{S_c}{\kappa_c} + x_s\frac{S_s}{\kappa_s}}{\frac{(1-x_s)}{\kappa_c} + \frac{x_s}{\kappa_s}} \quad (7)$$

$$\rho = (1 - x_s)\rho_c + x_s\rho_s \quad (8)$$

Here,  $x_s$  is the volume fraction of the “insulating” shell and  $S_s$  ( $S_c$ ) and  $\kappa_s$  ( $\kappa_c$ ) are the  $S$  and  $\kappa$  of the shell (core).  $\kappa$  does not change much upon reduction in 5%  $H_2$  (see Fig. 1) and  $\kappa \sim 2.5 \text{ W m}^{-1} \text{ K}^{-1}$  was assumed for both the core and shell regions. The measured  $S$  and  $\rho$  are therefore volume weighted averages of the core and shell regions. In order to evaluate the thermoelectric properties of the  $Sr_{0.20}La_{0.53}\square_{0.27}Ti_{1-y}Nb_yO_{3-\delta}$  samples reported here, we use the near universal  $S(\rho)$  relationship that exists for conducting La and Nb substituted  $SrTiO_3$  crystals.<sup>49-50</sup> The variation in  $S$  spans 1-2 orders of magnitude (10s-1000s  $\mu\text{V K}^{-1}$ ), while  $\rho$  varies by 4-5 orders of magnitude. The impact of the shell is therefore much more pronounced on  $\rho$  than it is on  $S$ . Previous work making an explicit comparison between single and polycrystalline  $Sr_{1-x}La_xTiO_3$  ( $x < 0.05$ ) suggested a  $\sim 70$  nm thick insulating acceptor layer.<sup>51</sup> Assuming a similar 50 nm insulating shell and cube shaped grains with  $10 \times 10 \times 10 \mu\text{m}^3$  dimensions, this leads to a 0.3 volume % fraction of shell material. Using the

measured  $S$ , and the  $S(\rho)$  relation this enables an estimate of  $\rho_c$  and of  $\rho_s$ , as summarized in Table 4. For the  $\text{Sr}_{0.20}\text{La}_{0.53}\square_{0.27}\text{Ti}_{1-y}\text{Nb}_y\text{O}_{3-\delta}$  samples, the values of  $\rho_s$  fall within a factor of five, between 8-40  $\Omega$  cm. This shows that the shell region remains reasonably conducting but is resistive enough to lead to a 1-2 order of magnitude increase in  $\rho$  at 300 K, thereby severely reducing the maximum attainable  $S^2/\rho$ . At higher temperatures, the impact of the insulating shell is reduced and  $\rho(T)$  takes its usual metal-like form and  $S^2/\rho$  is 50-60% reduced compared to samples without vacancies.

The near room temperature semiconducting  $\rho(T)$  can be used to obtain an estimate of the  $E_A$  for carrier transport through the shell. Inspection of a  $\log\rho(1/T)$  plot for the  $\text{Sr}_{0.20}\text{La}_{0.53}\square_{0.27}\text{Ti}_{1-y}\text{Nb}_y\text{O}_{3-\delta}$  samples reveals linear, thermally activated, behaviour between 300-580 K for the most insulating ( $y = 0$ ,  $y = 0.15$ ) samples, and 300-380 K for the more conducting  $y = 0.05$  and  $y = 0.1$  samples (Fig. S5). The  $y = 0$  sample was found to have  $E_A = 0.147(3)$  eV, while the Nb substituted samples have similar  $E_A = 0.098(3)$  eV (Table S1). We note that these values are much lower than observed from immittance spectroscopy on samples sintered in air ( $E_A \sim 1.4$  eV), where the shell is truly insulating. This analysis also suggests that the presence of Nb to some degree prevents the formation of the insulating shell upon cooling the samples.

## Discussion

*Thermal transport:* Low-temperature  $\kappa(T)$  data confirms the presence of a vacancy induced phonon-glass state, while  $C_p$  fitting demonstrates a transfer of spectral weight into a  $\omega_E \sim 120$   $\text{cm}^{-1}$  Einstein mode ( $\omega_E$ ), which is centred on a line of dispersion observed in the first principles phonon calculations and whose character is dominated by Sr displacements. Symmetry analysis was used to visualise the low-energy modes at the high-symmetry points and these are indeed dominated by Sr motions (Figure 2). The change in  $C_p$  signals a significant localisation of the heat carrying phonon modes upon the introduction of A-site vacancies, consistent with the removal of a large fraction (27%) of the Sr-O chemical bonds, leading to a flattening of the Sr dominated phonon modes. The

experimental data therefore indicates that the breaking of chemical bonds underpins the observed phonon-glass state, and that it is not only attributable to mass disorder in an otherwise “rigid” phonon band structure. The residual disorder that is apparent from the thermal displacement parameters affects all atomic sites, with the largest  $d^2$  for the nearest neighbour to the vacancy (O), followed by Ti and then Sr/La. This is in keeping with recent high-resolution STEM imaging that reveals that all sites are affected by the introduction of A-site vacancies.<sup>29</sup> The interpretation of this residual disorder is in terms of static displacements from the equilibrium position that are enabled by the removal of many of the Sr atoms. This disorder will impact on  $\kappa(T)$  but the magnitude of the displacements ( $d < 0.11 \text{ \AA}$  for O at 2 K) remains small, in particular compared to thermal motion at elevated temperatures, where the glass state survives, so cannot be the dominant contribution to reduction of  $\kappa(T)$ .

*Electrical:* Both impedance and DC electrical measurements reveal the presence of core-shell grain structures, which increase  $\rho$  and limit  $S^2/\rho$ . Removal of these oxidised shell regions will significantly enhance the thermoelectric performance, particularly at medium temperatures (450-500 K), where  $S^2/\rho$  usually peaks. At high-temperatures ( $> 600\text{-}700 \text{ K}$ ),  $\rho(T)$  returns to the metal-like dependence that is expected for degenerately doped  $\text{SrTiO}_3$ , and the impact of the insulating shell is much reduced with a 50-60% reduction compared to good polycrystalline samples. A-site vacancies open-up the perovskite structure and increase oxide ion conductivity.<sup>52</sup> It is therefore perhaps unsurprising that the formation of an insulating shell is exacerbated in samples with higher concentrations of A-site vacancies. Indeed, as discussed in the introduction, 5%  $\text{H}_2$  reduced samples with no and 7% vacancies do not show the near room temperature semiconducting tail, while samples with 13% and 27% vacancies do. Removal of the oxidised shells will enable strongly improved  $S^2/\rho$  near 500 K, while the gain at high-temperatures is expected to be smaller. It will thus help with creating a larger temperature-averaged power factor and broader high-ZT plateau, both of which are key features in improving power output and efficiency of a thermoelectric device. This work demonstrates that during cooling from sintering conditions in a 5%  $\text{H}_2$  in  $\text{N}_2$  atmosphere, the

oxygen partial pressure increases sufficiently for an oxidized shell to form at intermediate temperatures, after which the sample is kinetically trapped in a non-equilibrium core-shell state. Formation of this layer could be prevented by buffering the  $pO_2$  upon cooling or rapid quenching of the samples.

To conclude, the phonon-glass state is not only a result of the large mass disorder created on the perovskite A-site, but can be linked directly to the removal of the Sr-O bonds, leading to localisation of specific low-energy heat carrying Sr-O phonon modes. Electrical properties are dominated by a heterogeneous core-shell grain microstructure, which limits the electrical conductivity and thus the power factor. If the grain boundary structure can be controlled, whilst maintaining the A-site defect chemistry, significant improvements in power factor and device figure of merit are possible.

### **Acknowledgements**

The EPSRC (EP/N01717X/1) and Leverhulme Trust (RPG-2012-576) are acknowledged for support and the STFC for provision of beam time at ISIS. Raw data underpinning this work is available from the Heriot-Watt data repository.

### **Supplementary Information**

Crystallographic information from Rietveld analysis of laboratory X-ray and neutron powder diffraction; laboratory X-ray powder diffraction patterns; Scanning Electron Microscopy data; additional immittance spectroscopy data and Arrhenius fits to the near room temperature DC electrical resistivity data.

**Table 1.** Symmetry-allowed atomic displacements (phonon character) at high-symmetry points of the Brillouin Zone (BZ) for a  $Pm-3m$   $ABO_3$  perovskite structure. The “X” indicates that displacements of that atom type are allowed by symmetry for that irreducible representation (IR). Note that the segregation between A and B site displacements is almost complete at the high-symmetry BZ points, indicating that A and B site motions are not coupled. Labels for the IRs are as tabulated in the web-based program ISODISTORT based on the  $Pm-3m$  perovskite structure with A  $1a$  (0,0,0), B  $1b$  ( $\frac{1}{2}$ ,  $\frac{1}{2}$ ,  $\frac{1}{2}$ ), O  $3c$  (0,  $\frac{1}{2}$ ,  $\frac{1}{2}$ ).

Irreducible Representations		A	B	O
[0 0 0]	$\Gamma_4^-$	X	X	X
	$\Gamma_5^-$	-	-	X
$[\frac{1}{2} \frac{1}{2} \frac{1}{2}]$	$R_5^+$	-	X	-
	$R_2^-$	-	-	X
	$R_3^-$	-	-	X
	$R_4^-$	X	-	X
	$R_5^-$	-	-	X
$[\frac{1}{2} \frac{1}{2} 0]$	$M_1^+$	-	-	X
	$M_2^+$	-	-	X
	$M_3^+$	-	-	X
	$M_4^+$	-	-	X
	$M_5^+$	-	-	X
	$M_2^-$		X	X
	$M_3^-$	X	-	-
	$M_5^-$	X	X	X
$[\frac{1}{2} 0 0]$	$X_1^+$	-	X	X
	$X_2^+$	-	-	X
	$X_5^+$	-	X	X
	$X_3^-$	X	-	X
	$X_5^-$	X	-	X

**Table 2.** Symmetry-allowed atomic displacements (phonon character) at lower symmetry lines of the Brillouin Zone (BZ) for a  $Pm-3m$   $ABO_3$  perovskite structure. The “X” indicates that displacements of that atom type are allowed by symmetry for that irreducible representation (IR). Note that motions of both A and B are now often symmetry allowed within an IR, leading to coupling between A, B and O site motions. Labels for the IRs are as tabulated in the web-based program ISODISTORT based on the  $Pm-3m$  perovskite structure with A  $1a$  (0,0,0), B  $1b$  ( $\frac{1}{2}$ ,  $\frac{1}{2}$ ,  $\frac{1}{2}$ ), O  $3c$  (0,  $\frac{1}{2}$ ,  $\frac{1}{2}$ ).

Irreducible Representations		A	B	O
[ $\frac{1}{2}$ $\frac{1}{2}$ $\gamma$ ]	T1	X	-	<b>X</b>
	T2	-	-	<b>X</b>
	T3	-	X	<b>X</b>
	T4	-	-	<b>X</b>
	T5	X	X	<b>X</b>
[ $\alpha$ $\frac{1}{2}$ $\alpha$ ]	S1	X	X	<b>X</b>
	S2	X	-	<b>X</b>
	S3	X	X	<b>X</b>
	S4	-	X	<b>X</b>
[ $\alpha$ $\alpha$ $\alpha$ ]	LD1	X	X	<b>X</b>
	LD2	-	-	<b>X</b>
	LD3	X	X	<b>X</b>
[ $\alpha$ $\alpha$ 0]	SM1	X	X	<b>X</b>
	SM2	X	X	<b>X</b>
	SM3	X	X	<b>X</b>
	SM4	-	-	<b>X</b>
[ $\alpha$ 0 0]	DT1	X	X	<b>X</b>
	DT2	-	-	<b>X</b>
	DT5	X	X	<b>X</b>
[ $\alpha$ $\frac{1}{2}$ 0]	Z1	X	X	<b>X</b>
	Z2	-	X	<b>X</b>
	Z3	X	X	-
	Z4	X	X	-

**Table 3.** Summary of heat capacity fitting parameters for SrTiO<sub>3</sub> and Sr<sub>0.2</sub>La<sub>0.53</sub>□<sub>0.27</sub>TiO<sub>3</sub> sintered in air, where  $\theta_{Di}$  and  $\theta_{Ei}$  are the energies in degrees Kelvin of the Debye and Einstein oscillators used in the fits and the n-values give their weightings.  $\gamma$  is the Sommerfeld coefficient in mJ mol<sup>-1</sup> K<sup>-2</sup>.

	$\gamma$	$\theta_{D1}$	$n_{D1}$	$\theta_{D2}$	$n_{D2}$	$\theta_{E1}$	$n_{E1}$	$\theta_{E2}$	$n_{E2}$	$n_{tot}$
SrTiO <sub>3</sub>	0.24(1)	676(3)	3.12(1)	249(1)	1.78(1)	166(1)	0.10(1)	19.2(1)	0.0009(1)	5.00
Sr <sub>0.2</sub> La <sub>0.53</sub> □ <sub>0.27</sub> TiO <sub>3</sub>	0.50(1)	617(5)	3.18(1)	223(1)	1.07(1)	175(1)	0.48(1)	17.2(1)	0.0009(1)	4.73

**Table 4.** The conducting core - insulating shell composite model applied to the  $\text{Sr}_{0.20}\text{La}_{0.53}\square_{0.27}\text{Ti}_{1-y}\text{Nb}_y\text{O}_{3-\delta}$  series sintered in 5%  $\text{H}_2$  in  $\text{N}_2$ . Here,  $\rho_{\text{core}}$  is estimated from the measured  $S$  using the near universal  $S(\rho)$  relationship for La and Nb doped  $\text{SrTiO}_3$ .<sup>49-50</sup> This affords an estimate of  $\rho_{\text{shell}}$ . All data at 450 K.

<b>y</b>	<b>S<sub>measured</sub> (<math>\mu\text{V K}^{-1}</math>)</b>	<b><math>\rho_{\text{measured}}</math> (<math>\text{m}\Omega \text{ cm}</math>)</b>	<b><math>\rho_{\text{core}}</math> (<math>\text{m}\Omega \text{ cm}</math>)</b>	<b><math>\rho_{\text{shell}}</math> (<math>\Omega \text{ cm}</math>)</b>
0	-205(5)	126(3)	1.8(1)	41.4(1)
0.05	-284(7)	29(1)	4.7(2)	8.1(1)
0.10	-234(6)	32(1)	2.8(1)	9.7(1)
0.15	-247(6)	80(2)	3.0(1)	25.7(1)

In all cases, 0.3 volume % fraction shell is assumed, corresponding to a 50 nm thick shell and cube shaped grains of  $10 \times 10 \times 10 \mu\text{m}^3$ . 2.5% estimated uncertainties on the measures  $S$  and  $\rho$  values.

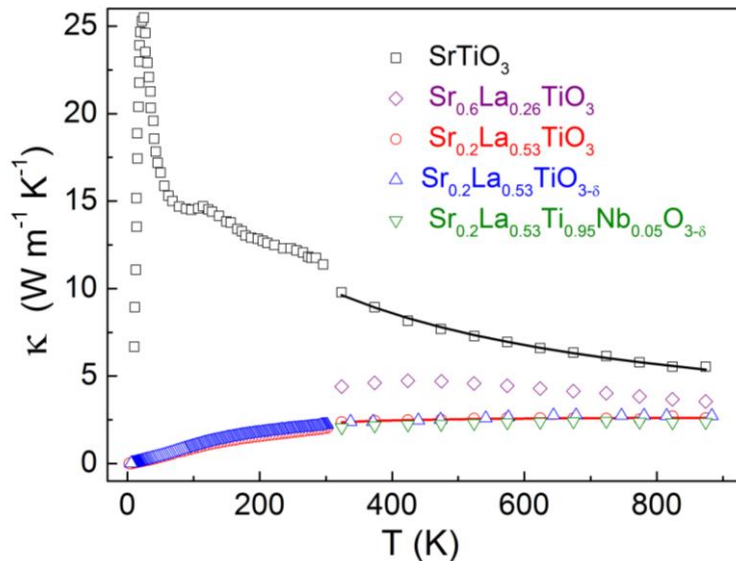


**Figure 1.** Temperature dependence of the thermal conductivity ( $\kappa$ ) for  $\text{SrTiO}_3$  with increasing amounts of A-site vacancies. The  $>300$  K data for the  $\text{Sr}_{1-x}\text{La}_{0.67x}\square_{0.33x}\text{TiO}_3$  ( $x = 0, 0.4$  and  $0.8$ ) samples sintered in air are reproduced from Ref. 22, while  $<300$  K literature data was used for  $\text{SrTiO}_3$ .<sup>53</sup> The solid lines  $>300$  K illustrate the transition from  $1/T$  (0% vacancies) to T-linear (27% vacancies) behaviour. The two samples with oxygen deficiency ( $\delta > 0$ ) were sintered in 5%  $\text{H}_2$  in  $\text{N}_2$ .

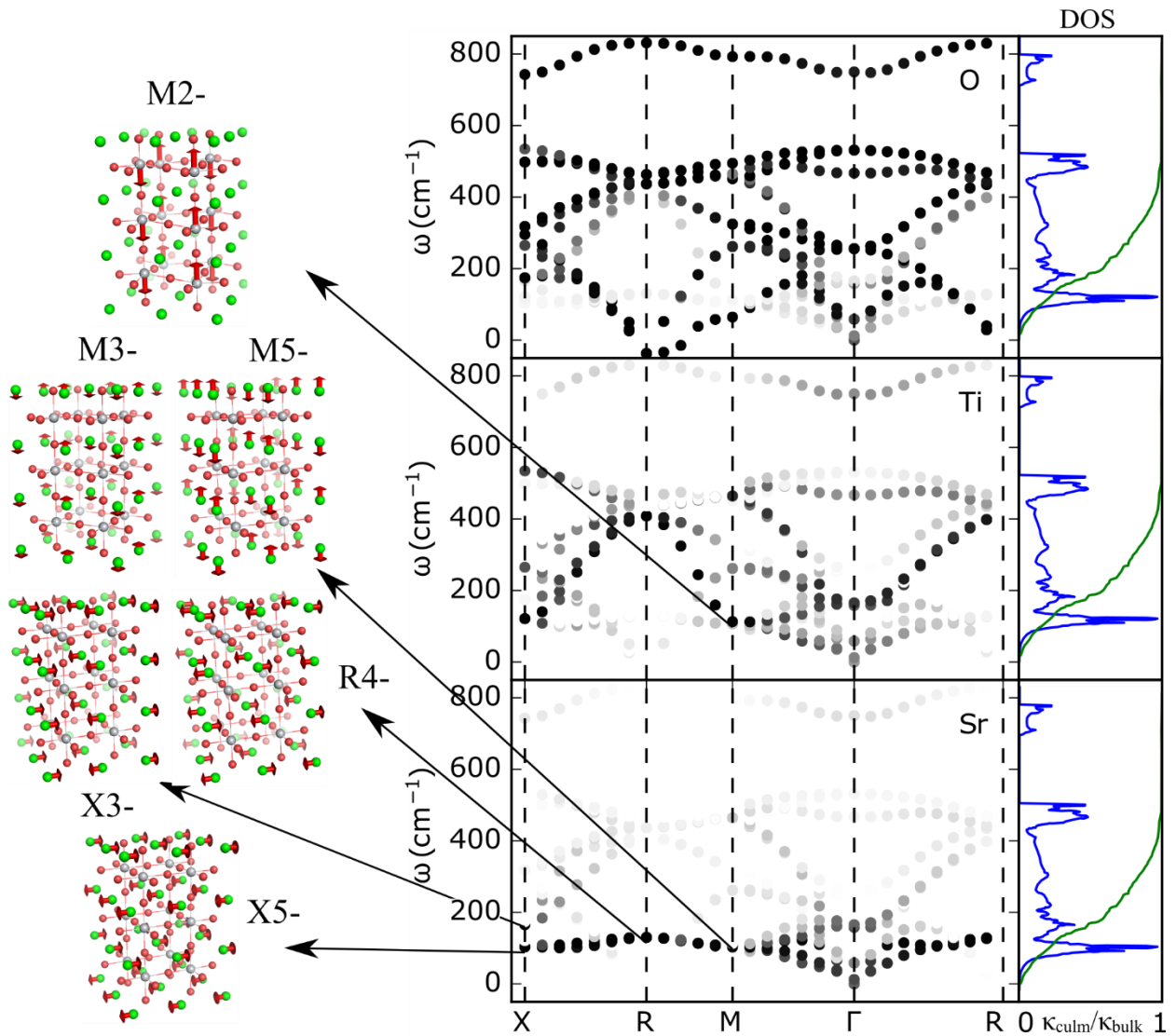


**Figure 2.** Phonon dispersion and atom resolved phonon dispersions for  $\text{SrTiO}_3$ , illustrating the low energy acoustic mode dominated by Sr at  $\sim 100 \text{ cm}^{-1}$ . The characters (atomic displacements) of the low-lying dispersion curves at high-symmetry points of the Brillouin Zone are illustrated on the left of the figures for phonon energies  $< 180 \text{ cm}^{-1}$ . Sr: Green; Ti: silver; O: red. The cumulative lattice conductivity at 300 K illustrates that the bulk of the thermal conductivity arises from the low-energy Sr-dominated modes. Data replotted from Feng et al. Ref. 37.

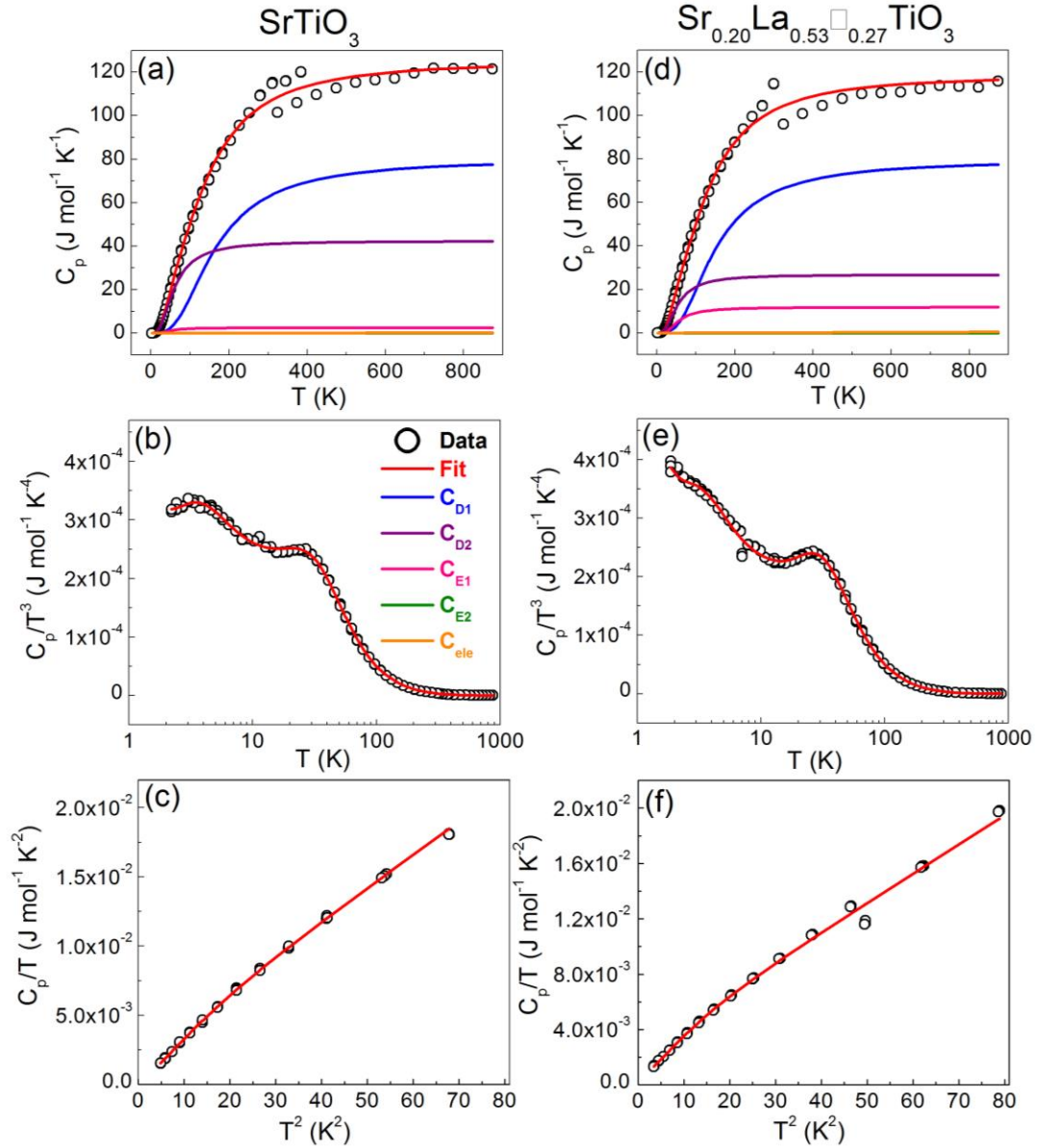


**Figure 3.** Heat capacity ( $C_p$ ) fitting for  $\text{SrTiO}_3$  and  $\text{Sr}_{0.2}\text{La}_{0.53}\square_{0.27}\text{TiO}_3$  sintered in air. Panels (a, d) show the direct fit to  $C_p$  using two Debye (D1, D2) and two Einstein terms (E1, E2) and an electronic contribution. Panels (b, e) show  $C_p/T^3$  versus  $T$ , highlighting the Einstein contribution at low temperatures. Panels (c, f) show  $C_p/T$  versus  $T^2$ , illustrating the non-linearity caused by the presence of the low energy Einstein mode, and the small but non-zero electronic Sommerfeld coefficient.

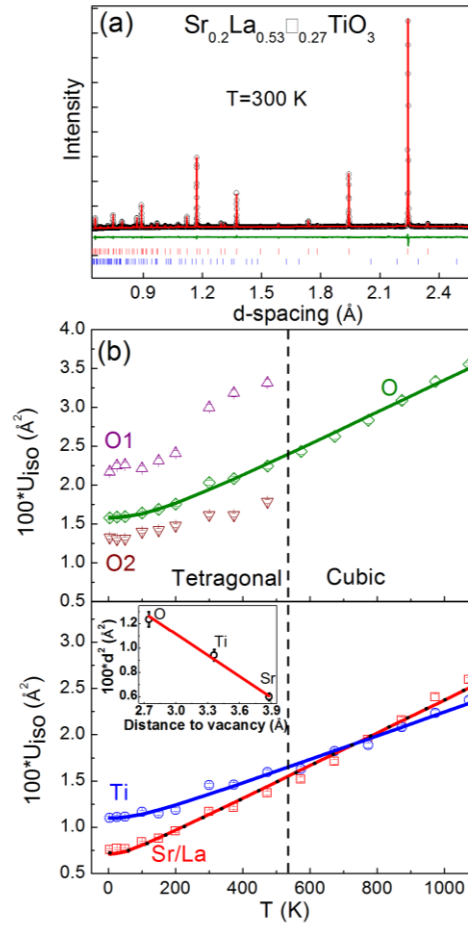


**Figure 4.** (a) Fitted neutron powder diffraction profile for  $\text{Sr}_{0.2}\text{La}_{0.53}\square_{0.27}\text{TiO}_3$  sintered in air. Black circles are the observed data, the red line is the calculated profile, and the green line is the difference curve. Selected superstructure reflections due to the transition to the  $I4/mcm$  structure with octahedral tilting are indicated by an asterisk. The Bragg markers are for the main phase (top line) and a 1wt%  $\text{TiO}_2$  secondary phase (bottom line). (b) Fits to the temperature dependence of the isotropic atomic displacement parameters ( $U_{\text{iso}}$ ) for the Sr/La, Ti and O sites in  $\text{Sr}_{0.2}\text{La}_{0.53}\square_{0.27}\text{TiO}_3$  as described in the text.

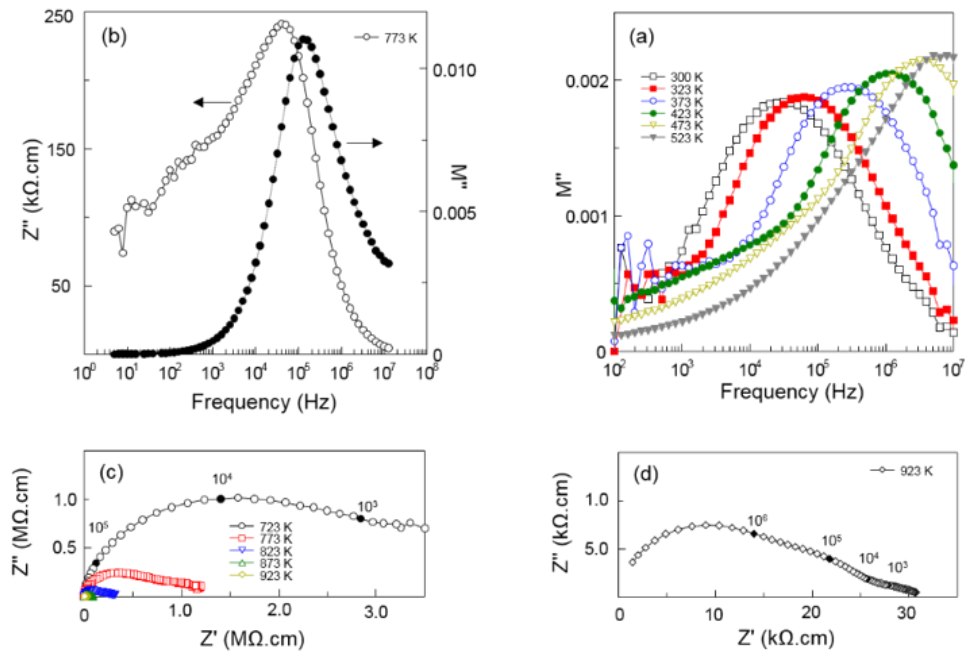


**Figure 5.** Immittance spectroscopy data as a function of temperature for  $\text{Sr}_{0.2}\text{La}_{0.53} \bullet 0.27\text{TiO}_3$  sintered in air: (a) imaginary modulus,  $M''$ , spectroscopic plot in the range 300-523 K indicating the conducting ‘core’ (region b1); (b) combined imaginary impedance ( $Z''$ ) and modulus ( $M''$ ) data at 773 K showing presence of a second insulating shell (region b2) response at higher temperature; (c, d) complex impedance ( $Z^*$ ) plane plots showing dominance of b2 to the total sample resistance but with contributions of grain boundary and electrode effects at lower frequency.

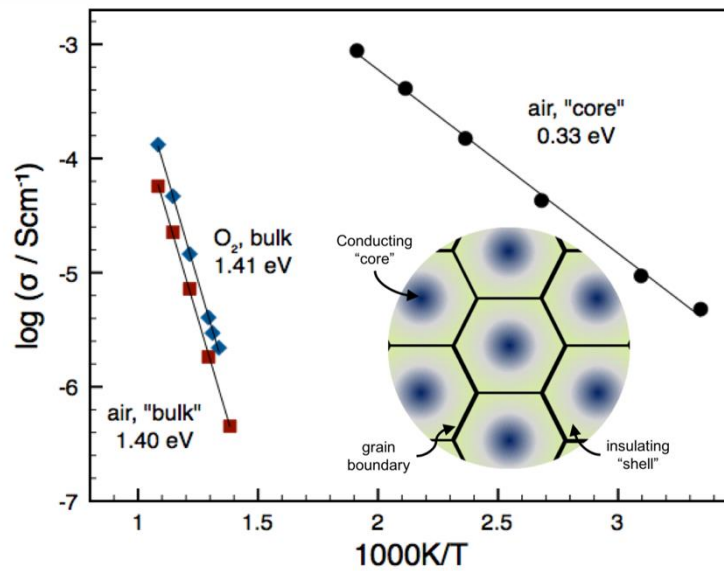


**Figure 6.** Arrhenius plot of conductivity of the semiconducting ‘core’ ( $\sigma_{b1}$  – filled circles) and insulating shell ( $\sigma_{b2}$  – filled squares) for  $\text{Sr}_{0.2}\text{La}_{0.53} \bullet 0.27\text{TiO}_3$  sample sintered in air, compared to the homogenous insulating bulk conductivity (filled diamonds) observed in the sample sintered in  $\text{O}_2$ . Calculated activation energies are also shown. Inset – schematic of the electrically inhomogeneous microstructure for the air-sintered composition.

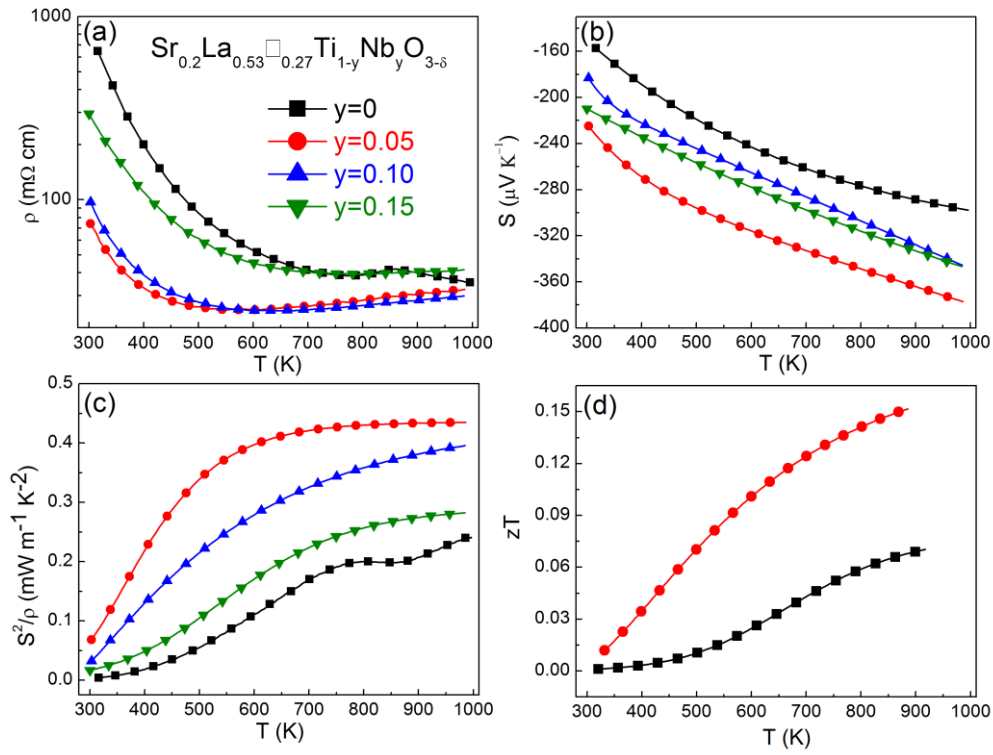


**Figure 7.** Temperature dependence of (a) the electrical resistivity ( $\rho$ ), (b) Seebeck coefficient ( $S$ ), (c) power factor ( $S^2/\rho$ ) and (d) the thermoelectric figure of merit,  $ZT$  for the  $\text{Sr}_{0.20}\text{La}_{0.53}\square_{0.27}\text{Ti}_{1-y}\text{Nb}_y\text{O}_{3-\delta}$  samples sintered in 5%  $\text{H}_2$  in  $\text{N}_2$ .

## References

1. Slack, G. A., In *CRC Handbook of Thermoelectrics*, Rowe, D. M., Ed. CRC Press: Boca Raton, 1995; p 407.
2. Rowe, D. M., *Thermoelectrics and its Energy Harvesting*. CRC Press: Boca Raton, 2012.
3. Snyder, G. J.; Toberer, E. S., Complex thermoelectric materials. *Nature Materials* **2008**, *7*, 105-114.
4. Nolas, G. S.; Cohn, J. L.; Slack, G. A.; Schujman, S. B., Semiconducting Ge clathrates: Promising candidates for thermoelectric applications. *Applied Physics Letters* **1998**, *73*, 178-180.
5. Cohn, J. L.; Nolas, G. S.; Fessatidis, V.; Metcalf, T. H.; Slack, G. A., Glasslike heat conduction in high-mobility crystalline semiconductors. *Physical Review Letters* **1999**, *82*, 779-782.
6. Sales, B. C.; Mandrus, D.; Williams, R. K., Filled skutterudite antimonides: A new class of thermoelectric materials. *Science* **1996**, *272*, 1325-1328.
7. Nolas, G. S.; Morelli, D. T.; Tritt, T. M., Skutterudites: A phonon-glass-electron crystal approach to advanced thermoelectric energy conversion applications. *Annual Review of Materials Science* **1999**, *29*, 89-116.
8. Toberer, E. S.; Zevalkink, A.; Snyder, G. J., Phonon engineering through crystal chemistry. *Journal of Materials Chemistry* **2011**, *21*, 15843-15852.
9. Christensen, M.; Abrahamsen, A. B.; Christensen, N. B.; Juranyi, F.; Andersen, N. H.; Lefmann, K.; Andreasson, J.; Bahl, C. R. H.; Iversen, B. B., Avoided crossing of rattler modes in thermoelectric materials. *Nature Materials* **2008**, *7*, 811-815.
10. Koza, M. M.; Johnson, M. R.; Viennois, R.; Mutka, H.; Girard, L.; Ravot, D., Breakdown of phonon glass paradigm in La- and Ce-filled Fe<sub>4</sub>Sb<sub>12</sub> skutterudites. *Nature Materials* **2008**, *7*, 805-810.

11. Kikuchi, A.; Okinaka, N.; Akiyama, T., A large thermoelectric figure of merit of La-doped SrTiO<sub>3</sub> prepared by combustion synthesis with post-spark plasma sintering. *Scripta Materialia* **2010**, *63*, 407-410.
12. Ohta, S.; Nomura, T.; Ohta, H.; Hirano, M.; Hosono, H.; Koumoto, K., Large thermoelectric performance of heavily Nb-doped SrTiO<sub>3</sub> epitaxial film at high temperature. *Applied Physics Letters* **2005**, *87*, 092108.
13. Lu, Z. L.; Zhang, H. R.; Lei, W.; Sinclair, D. C.; Reaney, I. M., High-Figure-of-Merit Thermoelectric La-Doped A-Site-Deficient SrTiO<sub>3</sub> Ceramics. *Chemistry of Materials* **2016**, *28*, 925-935.
14. Kovalevsky, A. V.; Yaremchenko, A. A.; Populoh, S.; Weidenkaff, A.; Frade, J. R., Enhancement of thermoelectric performance in strontium titanate by praseodymium substitution. *Journal of Applied Physics* **2013**, *113*.
15. Kovalevsky, A. V.; Yaremchenko, A. A.; Populoh, S.; Thiel, P.; Fagg, D. P.; Weidenkaff, A.; Frade, J. R., Towards a high thermoelectric performance in rare-earth substituted SrTiO<sub>3</sub>: effects provided by strongly-reducing sintering conditions. *Physical Chemistry Chemical Physics* **2014**, *16*, 26946-26954.
16. Yaremchenko, A. A.; Populoh, S.; Patricio, S. G.; Macias, J.; Thiel, P.; Fagg, D. P.; Weidenkaff, A.; Frade, J. R.; Kovalevsky, A. V., Boosting Thermoelectric Performance by Controlled Defect Chemistry Engineering in Ta-Substituted Strontium Titanate. *Chemistry of Materials* **2015**, *27*, 4995-5006.
17. Dehkordi, A. M.; Bhattacharya, S.; Darroudi, T.; Graff, J. W.; Schwingenschlogl, U.; Alshareef, H. N.; Tritt, T. M., Large Thermoelectric Power Factor in Pr-Doped SrTiO<sub>3-d</sub> Ceramics via Grain-Boundary-Induced Mobility Enhancement. *Chemistry of Materials* **2014**, *26*, 2478-2485.
18. Lin, Y.; Norman, C.; Srivastava, D.; Azough, F.; Wang, L.; Robbins, M.; Simpson, K.; Freer, R.; Kinloch, I. A., Thermoelectric Power Generation from Lanthanum Strontium

- Titanium Oxide at Room Temperature through the Addition of Graphene. *ACS Applied Materials & Interfaces* **2015**, *7*, 15898-15908.
19. Okuda, T.; Nakanishi, K.; Miyasaka, S.; Tokura, Y., Large thermoelectric response of metallic perovskites:  $\text{Sr}_{1-x}\text{La}_x\text{TiO}_3$  ( $0 < x < 0.1$ ). *Physical Review B* **2001**, *63*, 113104.
  20. Ohta, S.; Nomura, T.; Ohta, H.; Koumoto, K., High-temperature carrier transport and thermoelectric properties of heavily La- or Nb-doped  $\text{SrTiO}_3$  single crystals. *Journal of Applied Physics* **2005**, *97*, 034106.
  21. Muta, H.; Kurosaki, K.; Yamanaka, S., Thermoelectric properties of reduced and La-doped single-crystalline  $\text{SrTiO}_3$ . *Journal of Alloys and Compounds* **2005**, *392*, 306-309.
  22. Popuri, S. R.; Scott, A. J. M.; Downie, R. A.; Hall, M. A.; Suard, E.; Decourt, R.; Pollet, M.; Bos, J. W. G., Glass-like thermal conductivity in  $\text{SrTiO}_3$  thermoelectrics induced by A-site vacancies. *RSC Advances* **2014**, *4*, 33720-33723.
  23. Kato, K.; Yamamoto, M.; Ohta, S.; Muta, H.; Kurosaki, K.; Yamanaka, S.; Iwasaki, H.; Ohta, H.; Koumoto, K., The effect of Eu substitution on thermoelectric properties of  $\text{SrTi}_{0.8}\text{Nb}_{0.2}\text{O}_3$ . *Journal of Applied Physics* **2007**, *102*, 116107.
  24. Yamamoto, M.; Ohta, H.; Koumoto, K., Thermoelectric phase diagram in a  $\text{CaTiO}_3$ - $\text{SrTiO}_3$ - $\text{BaTiO}_3$  system. *Applied Physics Letters* **2007**, *90*, 072101.
  25. Fukuyado, J.; Narikiyo, K.; Akaki, M.; Kuwahara, H.; Okuda, T., Thermoelectric properties of the electron-doped perovskites  $\text{Sr}_{1-x}\text{Ca}_x\text{Ti}_{1-y}\text{Nb}_y\text{O}_3$ . *Physical Review B* **2012**, *85*, 075112.
  26. Wang, Y. F.; Fujinami, K.; Zhang, R. Z.; Wan, C. L.; Wang, N.; Ba, Y. S.; Koumoto, K., Interfacial Thermal Resistance and Thermal Conductivity in Nanograined  $\text{SrTiO}_3$ . *Applied Physics Express* **2010**, *3*, 031101.
  27. Popuri, S. R.; Bos, J. W. G., A-Site Deficient  $\text{SrTiO}_3$ : A Possible Phonon-Glass Electron-Crystal? *MRS Advances* **2016**, *1*, 3997-4002.
  28. Jackson, S. S.; Azough, F.; Freer, R., Neodymium-Strontium Titanate: A New Ceramic for an Old Problem. *Journal of Electronic Materials* **2014**, *43*, 2331-2336.

29. Azough, F.; Jackson, S. S.; Ekren, D.; Freer, R.; Molinari, M.; Yeandel, S. R.; Panchmatia, P. M.; Parker, S. C.; Maldonado, D. H.; Kepaptsoglou, D. M.; Ramasse, Q. M., Concurrent La and A-Site Vacancy Doping Modulates the Thermoelectric Response of SrTiO<sub>3</sub>: Experimental and Computational Evidence. *ACS Applied Materials & Interfaces* **2017**, *9*, 41988-42000.
30. Kovalevsky, A. V.; Yaremchenko, A. A.; Populoh, S.; Weidenkaff, A.; Frade, J. R., Effect of A-Site Cation Deficiency on the Thermoelectric Performance of Donor-Substituted Strontium Titanate. *Journal of Physical Chemistry C* **2014**, *118*, 4596-4606.
31. Daniels, L. M.; Savvin, S. N.; Pitcher, M. J.; Dyer, M. S.; Claridge, J. B.; Ling, S.; Slater, B.; Cora, F.; Alaria, J.; Rosseinsky, M. J., Phonon-glass electron-crystal behaviour by A site disorder in n-type thermoelectric oxides. *Energy & Environmental Science* **2017**, *10*, 1917-1922.
32. Toby, B. H., EXPGUI, a graphical user interface for GSAS. *Journal of Applied Crystallography* **2001**, *34*, 210-213.
33. Campbell, B. J.; Stokes, H. T.; Tanner, D. E.; Hatch, D. M., ISODISPLACE: a web-based tool for exploring structural distortions. *Journal of Applied Crystallography* **2006**, *39*, 607-614.
34. Clark, S. J.; Segall, M. D.; Pickard, C. J.; Hasnip, P. J.; Probert, M. J.; Refson, K.; Payne, M. C., First principles methods using CASTEP. *Zeitschrift Fur Kristallographie* **2005**, *220*, 567-570.
35. Refson, K.; Tulip, P. R.; Clark, S. J., Variational density-functional perturbation theory for dielectrics and lattice dynamics. *Physical Review B* **2006**, *73*, 155114.
36. Perdew, J. P.; Ruzsinszky, A.; Csonka, G. I.; Vydrov, O. A.; Scuseria, G. E.; Constantin, L. A.; Zhou, X. L.; Burke, K., Restoring the density-gradient expansion for exchange in solids and surfaces. *Physical Review Letters* **2008**, *100*, 136406.

37. Feng, L.; Shiga, T.; Shiomi, J., Phonon transport in perovskite SrTiO<sub>3</sub> from first principles. *Applied Physics Express* **2015**, *8*, 071501.
38. Ashcroft, N. W.; Mermin, N. D., *Solid State Physics*. Thomson Learning: 1976.
39. Howard, C. J.; Stokes, H. T., Group-theoretical analysis of octahedral tilting in perovskites. *Acta Crystallographica Section B-Structural Science* **1998**, *54*, 782-789.
40. Battle, P. D.; Bennett, J. E.; Sloan, J.; Tilley, R. J. D.; Vente, J. F., A-site cation-vacancy ordering in Sr<sub>1-3x/2</sub>La<sub>x</sub>TiO<sub>3</sub>: A study by HRTEM. *Journal of Solid State Chemistry* **2000**, *149*, 360-369.
41. Howard, C. J.; Lumpkin, G. R.; Smith, R. I.; Zhang, Z. M., Crystal structures and phase transition in the system SrTiO<sub>3</sub>-La<sub>2/3</sub>TiO<sub>3</sub>. *Journal of Solid State Chemistry* **2004**, *177*, 2726-2732.
42. Willis, B. T. M.; Bertram, T. M.; Pryor, A. W., *Thermal Vibrations in Crystallography*. Cambridge University Press: 1975.
43. Popuri, S. R.; Pollet, M.; Decourt, R.; Viciu, M. L.; Bos, J. W. G., Evidence for hard and soft substructures in thermoelectric SnSe. *Applied Physics Letters* **2017**, *110*, 253903.
44. Irvine, J. T. S.; Sinclair, D. C.; West, A. R., Electroceramics: Characterization by Impedance Spectroscopy. *Advanced Materials* **1990**, *2*, 132-138.
45. Morrison, F. D.; Sinclair, D. C.; West, A. R., Characterization of Lanthanum-Doped Barium Titanate Ceramics Using Impedance Spectroscopy. *Journal of the American Ceramic Society* **2001**, *84*, 531-538.
46. Reaney, I. M.; Iddles, D., Microwave Dielectric Ceramics for Resonators and Filters in Mobile Phone Networks. *Journal of the American Ceramic Society* **2006**, *89*, 2063-2072.
47. Sinclair, D. C.; Adams, T. B.; Morrison, F. D.; West, A. R., CaCu<sub>3</sub>Ti<sub>4</sub>O<sub>12</sub>: One-step internal barrier layer capacitor. *Applied Physics Letters* **2002**, *80*, 2153-2155.
48. Gelbstein, Y., Thermoelectric power and structural properties in two-phase Sn/SnTe alloys. *Journal of Applied Physics* **2009**, *105*, 023713.

49. Bouzerar, G.; Thebaud, S.; Adessi, C.; Debord, R.; Apreutesei, M.; Bachelet, R.; Pailhes, S., Unified modelling of the thermoelectric properties in SrTiO<sub>3</sub>. *EPL* **2017**, *118*.
50. Kang, S. D.; Dylla, M.; Snyder, G. J., Thermopower-conductivity relation for distinguishing transport mechanisms: Polaron hopping in CeO<sub>2</sub> and band conduction in SrTiO<sub>3</sub>. *Physical Review B* **2018**, *97*, 235201.
51. Moos, R.; Hardtl, K. H., Electronic transport properties of Sr<sub>1-x</sub>La<sub>x</sub>TiO<sub>3</sub> ceramics. *Journal of Applied Physics* **1996**, *80*, 393-400.
52. Neagu, D.; Irvine, J. T. S., Structure and Properties of La<sub>0.4</sub>Sr<sub>0.4</sub>TiO<sub>3</sub> Ceramics for Use as Anode Materials in Solid Oxide Fuel Cells. *Chemistry of Materials* **2010**, *22*, 5042-5053.
53. Buscaglia, M. T.; Maglia, F.; Anselmi-Tamburini, U.; Marré, D.; Pallecchi, I.; Ianculescu, A.; Canu, G.; Viviani, M.; Fabrizio, M.; Buscaglia, V., Effect of nanostructure on the thermal conductivity of La-doped SrTiO<sub>3</sub> ceramics. *Journal of the European Ceramic Society* **2014**, *34*, 307-316.

TOC image

